

POLITECNICO DI TORINO  
Repository ISTITUZIONALE

DESIGN OF A PROTOTYPE UNMANNED LIGHTER-THAN-AIR PLATFORM FOR REMOTE SENSING:

*Original*

DESIGN OF A PROTOTYPE UNMANNED LIGHTER-THAN-AIR PLATFORM FOR REMOTE SENSING:  
CONTROL, ALIMENTATION, AND PROPULSION SYSTEMS / Gili, Piero; Civera, Marco; Roy, Rinto; Cibrario Bertolotti, Samuele; Cosenza, Davide; Gili, Alfredo; Surace, Cecilia. - STAMPA. - (2021). ( 32 nd ICAS 2021 Shanghai Cina 6-10 settembre 2021).

*Availability:*

This version is available at: 11583/2949072 since: 2022-01-11T17:51:42Z

*Publisher:*

ICAS

*Published*

DOI:

*Terms of use:*

This article is made available under terms and conditions as specified in the corresponding bibliographic description in the repository

*Publisher copyright*

(Article begins on next page)

## DESIGN OF A PROTOTYPE UNMANNED LIGHTER-THAN-AIR PLATFORM FOR REMOTE SENSING: CONTROL, ALIMENTATION, AND PROPULSION SYSTEMS

P. Gili<sup>1,3</sup>, M. Civera<sup>1,3</sup>, R. Roy<sup>1</sup>, S. Cibrario Bertolotti<sup>1</sup>, D. Cosenza<sup>1</sup>, A. Gili<sup>1</sup>, & C. Surace<sup>2,3</sup>

<sup>1</sup> Department of Mechanical and Aerospace Engineering, Politecnico di Torino, Turin, Italy

<sup>2</sup> Department of Structural, Geotechnical and Building Engineering, Politecnico di Torino, Turin, Italy

<sup>3</sup> Interdepartmental Responsible Risk Resilience Centre (R3C), Politecnico di Torino, Turin, Italy

### Abstract

This work presents several aspects related to the design of a new concept for a Remotely Piloted Aircraft System (RPAS), specifically, a Lighter-Than-Air (LTA) platform for the remote sensing of medium-sized rural and urban areas. The airship's payload is intended to carry an array of sensors ranging from high-definition video cameras to hyperspectral sensors, a thermographic camera, and a LiDAR system, which all require power alimentation during low-speed surveying for fine mapping. Here, a fuel cell design solution, combined with supercapacitors, is proposed. The system is designed to provide energy for both the onboard sensors and the propulsion and thrust vector control system. In this regard, the design and optimization of the propeller blades, using Blade Element Momentum Theory (BEMT), is discussed as well, in a multidisciplinary optimisation fashion. A twin paper describes the other structural aspects of the airship design.

**Keywords:** Airship Design; Fuel Cells; Blade Element Momentum Theory; Remotely Piloted Aircraft System; Lighter-Than-Air Platform.

### 1. Introduction.

Any Lighter-Than-Air (LTA) platform, commonly referred to as an airship, can be simplified to a balloon moved by a propeller. Obviously, the shape of said balloon is properly modified to minimize the drag force generated by its movement and to maximize control properties. The structure must be reinforced to sustain load due to aerodynamic forces and propulsive forces generated by the propulsion system. Moreover, the balloon must be able to control its internal pressure to increase or decrease the altitude at which it is flying. This last function can be done by components called ballonets, which regulate the total pressure by inflating or deflating using a lighter-than-air gas, which is usually helium.

Although airships are not used anymore to transport passengers, except for rare exceptions, they are still very relevant in the fields of remote sensing, telecommunication, and security. Since these type of operations requires hovering in-place or slow movements, airships are a solid solution because they can accomplish these tasks by spending a minimum amount of power and, consequently, operative costs. Moreover, airships can carry heavy payloads (for example, this work investigates a case where the payload weights ~100 kg), therefore they can transport all the necessary instruments and sensors.

The types of propulsion and onboard energy systems used have varied through time and according to the mission that the airship is required to accomplish. Historically internal combustion motors were the main source of power, while today a full electric configuration is also possible using solar panels, batteries, supercapacitors, fuel cells, and electric motors.

For example, for missions lasting very long times (even months) and operating at stratospheric altitudes, the best way to produce power is mainly through solar panels because at this operating altitude there are no atmospheric phenomena able to block the sunlight and storing energy through fuel tanks would require an exorbitant amount of volume [1]. However, such high-altitude LTA solutions for persistent monitoring fall beyond the aims of this research, which rather focuses on local solutions for surveying at the small-to-medium urban/rural scale.

In modern solutions, the onboard energy system is rarely composed of only one type of energy source, but it is rather a hybrid solution that uses different sources, to cover the reciprocal weaknesses [2]. For the control and manoeuvring system, while in the past many solutions were based on aerodynamic control surfaces, the one studied in this work, as many other modern airships, uses vectored thrust.

## 2. The Proposed Airship Concept.

Traditional airships fall into three categories: pressurized, rigid, and semi-rigid. Pressurized ones use a small differential pressure between the lifting gas inside the hull to maintain their form and an internal system of tie rods that convey the load to the envelope of the airship. These are also commonly known as blimps. On the contrary, rigid ones are formed by a skeletal rigid structure that contains the gas in internal compartments. Semi-rigid airships are similar to pressurized ones, but with a structural keel that absorbs part of the aerodynamic loads [3]. A pressurized configuration would require an impractical balloon thickness, and be incapable of correctly stabilizing motors, while a rigid one would result in a higher structural density, requiring larger balloons to sustain the payload weight. So, a semi-rigid architecture has been adopted for the present work. Specifically, the proposed design includes a pressurized lifting gas balloon, surrounded by an adherent keel. The propulsion system is composed of a set of six motors directly connected to the keel, that provides support and stability, absorbing their thrust. A set of four semi-spherical legs provide the stability needed on the ground and a rigid platform positioned under the belly of the airship locates the payload and energy systems.

The propulsion system is composed of six electrical propeller engines, driven by polyphase alternating current motors, connected to the energy system via cables allocated inside the keel. This solution will be referred to hereinafter as the 'thrust vector' control system. The main reason behind this choice is the requirement of zero-emission by the airship. Four of these engines, the ones above and below the keel, are mounted on stepper motors, which provides them with the mobility needed to direct the aircraft. The other two provide vertical thrust and help controlling altitude.

The payload system allocates all the sensors needed for the mission, mounted on a three-axis stabilizing platform. Auxiliary to the payload system the On-Board Computer (OBC) manages the communication with the ground station and the control of the airship. The energy system stores and provides energy to all the other systems and is one of the most impactful on airship optimization.

Figure-1 provides a general overview of the proposed LTA.

To properly size the LTA structure, a quite complicated balance between the weight of the several components needs to be reached. Here and in a twin paper [4], the approach followed was one of multidisciplinary design optimisation. The several subroutines will be detailed in the following sections; the complete procedure will be summarised at the end of this paper.



Figure 1 – Qualitative 3D rendering of the airship during flight (with the landing gear rotated inward).

The classic balloon shape, an axisymmetric, egg-shaped hull, modelled by two ellipsoids halves, is adopted to easily estimate drag and weight [5]. The general equation of the fuse longitudinal section (Equation-1) follows the National Physical Laboratory (NPL) shape, which also provides relations for

the relative thickness (Equation-2) and balloon length (Equation-3); that is substantially the airship length.

$$y = \pm b \sqrt{1 - \frac{(x-a)^2}{a^2}} \text{ for } x \leq a \quad (1)$$

$$y = \pm b \sqrt{1 - \frac{(x-a)^2}{2a^2}} \text{ for } x > a$$

$$\left(\frac{d}{l}\right) = \frac{2b}{l} \quad (2)$$

$$l = (1 + \sqrt{2})a \quad (3)$$

The empirical Hoerner formula (Equation-4) supposes a turbulent flow around the hull and provides accurate values of the drag coefficient  $C'_{DV}$  of this shape up to relative thickness ( $d/l$ ) values of 0.32-0.33 [6]. The drag coefficient is defined relative to a reference surface (Equation-5), as a function of the balloon's volume  $V$ , while the Reynolds number  $Re$  uses a reference length (Equation-6).

$$C'_{DV} = \frac{0.171 \left(\frac{d}{l}\right)^{-\frac{1}{3}} + 0.252 \left(\frac{d}{l}\right)^{1.2} + 1.031 \left(\frac{d}{l}\right)^{2.7}}{Re^{\frac{1}{6}}} \quad (4)$$

$$S_{ref} = V^{\frac{2}{3}} \quad (5)$$

$$L_{ref} = V^{\frac{1}{3}} \quad (6)$$

The dimensioning code uses Equations-4, 5, and 6 to estimate the optimal balloon dimension, as explained in a later section of this paper.

## 2.1 Onboard Sensing Systems.

The onboard sensing system of the airship is primarily composed of two different payloads: a data payload and a support payload. The first primary function is to collect data for future analysis, while the latter carries out essential functions for the data collecting sensors indirectly.

The data payload is composed of a photogrammetric camera, a thermal camera, a LiDAR scanner, and a hyperspectral camera. The support one is composed of a three-axis stabilizing platform, an onboard computer and data storage device, a GPS/INS system, and eventually thermal components.

The three-axis stabilizing platform is essential to maintain the correct orientation of the instruments against the oscillation of the airship. The onboard computer stores data arriving from the data payload and manages the connection with the ground controller. The GPS/INS system is essential for the calibration of some of the data payload sensors, while thermal components maintain payload instruments in their temperature operational range.

**Photogrammetry Camera.** A photogrammetry camera is a traditional digital camera, operating in the visible spectrum of light, used to acquire a sequence of aerial images at relatively low altitudes. Images are collected with a very high forward and spatial overlap (around 80%), and at a very high resolution. Correlated with information from the GPS/INS system, these images can be used to obtain, via dedicated software, precise spatial maps or information, such as Digital Ortho Map (DOM), Digital Surface Models (DMS), and large-scale three-dimensional models. This kind of analysis is particularly demanding on maximum scanning altitude and flight strips distance, due to the resolution and overlap requirements, and results in one of the most limiting factors to be considered in the entire sensor payload. Due to this restriction to optical radiations, a clear view of the landscape is required to correctly operate this camera, limiting even further the altitude range of operability under the altitude of the clouds, at around 600 m, and weather operability to the bright hours of the day [7][8].

**Thermal Camera.** A thermal camera is a camera operating in the infrared spectrum of light. Images collected need to provide a good spatial resolution to obtain significant data, for example, Ren et. al. [9] pointed out that a resolution of 0.8 m provides good quality for the analysis. Thermal images, correlated with precise position provided by the GPS/INS system, and corresponding images from the photogrammetry camera can be processed to obtain spatial referenced thermal data, such as the

Land Surface Temperature (LST) pattern or the Surface Urban Heat Island (SUHI). Maps of this kind are particularly useful to recognize areas at high risk of fire and monitor the urban thermal environment. Thermal cameras have a very low field of view, and require a considerable overlap to obtain significant data, thus rendering this sensor the most limiting one in terms of flight strips distance, requiring a very packed serpentine. Thermal cameras, as photogrammetry ones, require a clear sky to work properly, due to the light scattering phenomena on small droplets that compose clouds and fog.

**LiDAR Scanner.** LiDAR scanners are complex instruments composed of a high-resolution Photogrammetry Camera, a GPS/INS unit, and a laser scanner unit. In our specific payload composition, the first two components are already used for different analyses, so only a laser scanner unit is required. The LiDAR scanner uses a laser to measure the time between the emission of the signal and its reflection by a surface, providing high-resolution 3D or 2D models of its target. The system is used prominently to obtain height maps of the objective terrain, to create a digital terrain/surface model (DTM/DSM), or highly accurate ortho-imagery. In opposition with other components, the LiDAR requires a moderate overlap (around 30%) to obtain reliable data, but despite having great accuracy in terms of points distance measured, it has limitations on the speed at which it can be moved to perform the analysis. The LiDAR has mechanical limitations on the angular speed of the scanning laser used to map the desired location. High airship speed results in low point density, thus in a less defined model of the surface. LiDAR scanners are also particularly sensitive to ground reflectiveness, resulting in a range reduction of almost  $\frac{1}{3}$  at 10% reflectivity in respect to the 80% reflectivity case [10,11].

**Hyperspectral Camera.** Hyperspectral camera is capable of capturing Hyperspectral imaging, i.e. to provide a picture where each pixel carries the information about the intensity of the radiation reflected by a surface for a certain number of spectral bands. Correlated with information of a GPS/INS system and photogrammetry the system can be used, with the proper post-processing program, to obtain a composition terrain map, that evaluates the differences in the reflective spectrum of different materials, the Leaf Area Index (LAI) and Land Use and Land Cover (LULC). With high-resolution data such as the ones provided by an airship, several parameters of the ground materials can be examined due to his low altitude. For example, a study by Liu et. al. [12] has shown that an airship mounted multispectral camera can provide information on water composition and pollution. Hyperspectral cameras require large overlaps to work properly, similar to that of a photogrammetry camera, and low airship speed, due to data rate limitations, and has a considerable weight that has to be considered [13-16].

With consideration of the ground resolution, scanning time, weight, and power absorbed the following roster of components, listed in Table-1, have been chosen in the preliminary phase.

Table 1 - Payload components data.

Sensing Device	Example of Commercially Available Model	Temperature Range (Operative)	Weight	Power Consumption
Photogrammetry Camera	Phase One ® iXM-RS150F	-10/+40 °C	2.15 kg (with 90 mm lens)	16 W
Thermal Camera	NEC ® TH9260	-15/+50 °C	1.70 kg	25 W
LiDAR Scanner	Optech ® ALTM Galaxy T1000	0/+35 °C	33.5 kg	300 W
Hyperspectral Camera	SPECIM ® AisaDUAL	+5/+40 °C	50.0 kg	600 W
OBC + Data Storage + GPS/IMU	-	+5/+40 °C	~10.0 kg	~250W
Total (including stabilizing platform, cabling, etc.)	-	+5/+40 °C	~100.0 kg	~1000 W

The chosen components reach an acceptable weight of around 100 kg and low power consumption of around 1 kW. Further analysis on the payload, to contain both the ground resolution and scanning time under the chosen values, shown in Figure-2, and to address more specific requirements, such as sensor maximum range, the necessity of a clear vision, thermal excursion with altitude according to the standard atmosphere (ISA) and components working ranges, the scanning working point of the airship in the scanning phase has been set to a speed of 13 m/s and an altitude of 500 m above ground.

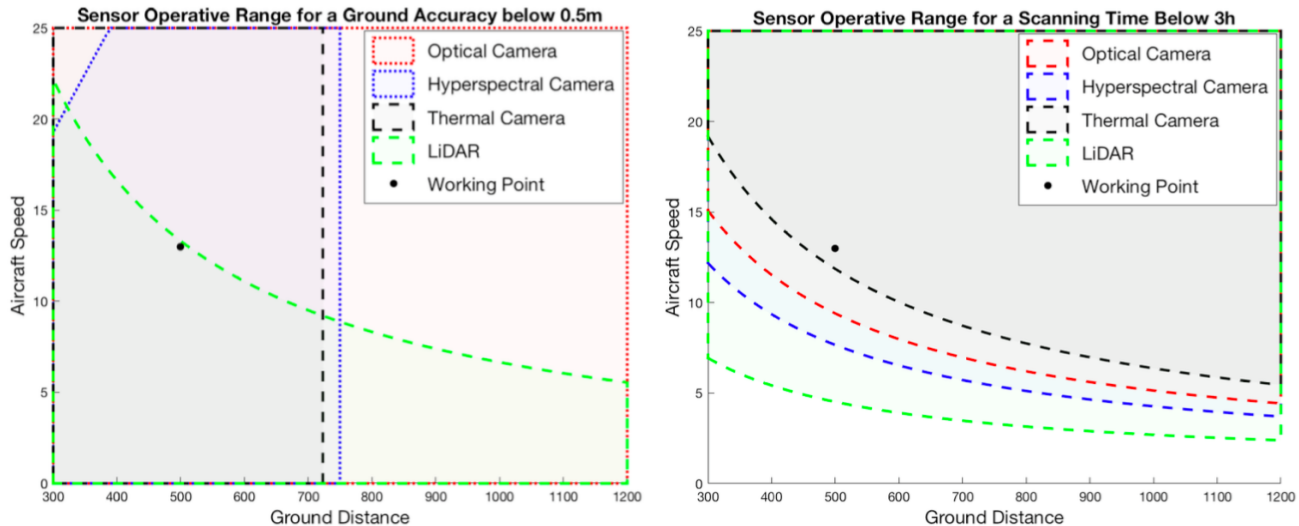


Figure 2 – Accuracy operative range (left), and scanning time operative range (right)

Another set of onboard sensing devices is dedicated for the structural health monitoring (SHM) and integrity assessment of the load-bearing components. These include wired and/or wireless Inertial Measurement Units (IMUs). The sensors are intended to capture and transmit the vibrational behaviour of the structure. Signal processing techniques such as e.g. Adaptive Mode Decomposition Methods [17] can be then used to isolate and extract information from these recordings. Fault-related anomalies can be thus detected as deviations from a data-driven normal operating conditions (NOCs) model (such as e.g. what performed in [18] or [19]) and used for risk assessment and failure analysis [20].

### 3. Onboard Energy System.

The purpose of the onboard energy system is to provide energy to all the components of the airship such as the payload and the propulsion system. This system must supply all the needed power during nominal navigation conditions and when a peak is requested the supercapacitors module provides it, regardless of the main technology used for the energy system. The most suitable ones for the kind of airship and missions considered by this study are the hydrogen fuel cells system and the battery system. A numerical code, which will be further described, was employed to determine which energy system is the most suitable depending on the distance of the airship from the measurement area.

The reason why electric power is chosen instead of a fossil fuel system to feed the propulsion system is that it produces a minimum amount of greenhouse gases, has a low heat signature, produces less noise and vibrations and is usually less expensive.

#### 3.1 Candidate 1: Fuel Cell System.

The first potential option considered was a fuel cell system. This is composed of two subsystems: the fuel cells themselves and the fuel storage and distribution subsystem. A fuel cell is a device that converts the chemical energy of the fuel into electric energy and heat without using thermal cycles.

The kind considered in this study is a PEM (Polymer Electrolyte Membrane) that uses hydrogen ( $H_2$ ) as fuel and oxygen ( $O_2$ ) as the oxidizing element. It is composed of a cathode, where the oxygen is passed, an anode, where the hydrogen is passed, and a polymeric electrolyte membrane with high proton conductivity. At the anode, a catalyst splits the hydrogen into protons and electrons, and while the protons pass through the membrane, the electrons are forced to pass through a circuit to produce electric power. This process produces, besides the aforementioned excessive heat, water that needs

to be expelled out of the fuel cell [21].

The principal advantages of using a PEM fuel cell are that they have a relatively high efficiency (it varies according to the temperature between 40% and 60%) and they are the most reliable and used in the transportation field. They are scalable, which means they can be organized into stacks that can be assembled into modules to obtain a high level of power. Another advantage is that their performances do not depend on the dimension of the load and of the system. They are also an environmentally friendly solution since the reaction between  $O_2$  and  $H_2$  does not produce  $CO_2$ , especially if the processes to obtain the fuel uses renewable sources. The main problems are connected to the fuel: it can be quite expensive, its storage capacity on the aircraft is limited and the tank containing  $H_2$  affects the total weight of the airship. Moreover, hydrogen is flammable, so it must be stored at low temperatures; this makes it difficult to create structures suitable for its transportation.

At standard temperature and pressure, the density of hydrogen is low (0.089 kg/m<sup>3</sup>), so to increase its density, it is usually compressed in a pressurized tank or stored at its liquid state in a cryogenic tank. The first solution was discarded because it would have required a closed and hermetically sealed system to keep the hydrogen at 6.15°K, which is the temperature that keeps  $H_2$  in the liquid state. Although the density of liquid hydrogen is higher than the one achievable by using compressed hydrogen, all the problems arising from the cooling system, such as the increase in weight caused by it and the difficulty to integrate it on the airship, have resulted in it being discarded [22]. The second solution consists of type IV tanks to store hydrogen compressed at 70 MPa: the increase in pressure causes an increase in its density. By doing so the volume needed to store the fuel is decreased. Type IV tanks are composite materials composed of thermoplastic elements and reinforcing fibres to bear the elevated pressure of the hydrogen inside. They can assume complex shapes, so they are easier to integrate into the structure of the airship [23]. The main problem connected with this technology is that it has a low gravimetric fraction, which is the ratio between the mass of the hydrogen stored and the mass of the storage system. However, this technology is still an object of study of many researchers, and since it has already been improved in the last years, it will probably be even more efficient in the future.

A ‘specific power’ (SP) is defined to determine the weight of the fuel cells when the power, which is the power that the energy system must supply, and the efficiency of the fuel cells are known. The value of SP was calculated from different commercial fuel cells and set at 500 W/kg [24]. Since the efficiencies of the fuel cells range between values of 40% and 60%, it is conservatively set equal to 45%. Therefore, the total mass of the fuel cells  $m_{fuel\ cell}$ , and the mass of hydrogen needed to provide the necessary power  $m_{H_2}$ , can be calculated using Equations-7 and 8,

$$m_{fuel\ cell} = \frac{P_n}{SP \cdot \eta} = \frac{P_n}{500 \cdot 0.45} \quad (7)$$

$$m_{H_2} = \frac{P_n \cdot t_f}{33330} \quad (8)$$

where  $t_f$  is the total duration of the flight (expressed in hours), and the specific energy of hydrogen is 33330 Wh/kg.

To calculate the weight of the tank and all the subsystems needed for its operation, the data calculated by the Argonne National Lab (ANL) referring to a 5.6 kg hydrogen tank were used [23]. The main components of this reference tank are listed in the following Table-2.

Table 2 - Hydrogen tank components.

Component	Mass
Stored $H_2$ (total/usable)	5.8/5.6 Kg
Composite (Fibre + Resin)	90.3 (67.1 + 23.2) Kg
Tank boss	0.9 Kg
HDPE liner	8.0 Kg
Integrated in-tank valve	3.0 Kg
Integrated regulator	3.6 Kg
Other	15.4 Kg

Using the values reported in Table-2 it is possible to determine the gravimetric fraction  $g_f$  with the following equation:

$$g_f = \frac{5.6}{105.8} = 0.053 \quad (9)$$

The term  $m_{variable}$  refers to the components whose mass varies with the mass of the hydrogen stored in the tanks, while the mass of the remaining components, called  $m_{fix}$  is approximately constant. So, the total mass of the generic empty tank system  $m_e$  is:

$$m_e = \frac{m_{H_2}}{g_f} + m_{fix} = \frac{m_{H_2}}{g_f} + 15.4 \quad (10)$$

As seen in Table-2, the total  $H_2$  stored is more than the actually usable mass. The ratio between these two quantities is supposed to be constant and equal to 0.966. The mass of the hydrogen stored in the tank ( $m_{H_2 tot}$ ) can be calculated using the following formula:

$$m_{H_2 tot} = \frac{m_{H_2}}{0.966} \quad (11)$$

### 3.2 Candidate 2: Batteries.

Another way to provide energy to the airship is through lithium-ion rechargeable batteries, which are widely used in the aeronautical field as well as for many other applications. They have a high energy density, around 250 Wh/kg, and usually work at voltages of about 4 V. Although they are not the lithium batteries with the highest rates of energy density, they are the only ones that have a long life cycle. For example, lithium-sulfur batteries have energy density values of 300-400 Wh/kg but they also have a very limited life cycle (less than 300 recharging cycles). Still, lithium-ion batteries are not perfect since they present energy losses during charging and recharging cycles and they suffer from the wear of the electrodes [25].

Lithium-ion batteries are composed of an anode and a cathode, both capable of storing lithium ions, a separating element between them, and a liquid electrolyte that fills the empty space of the battery. During the discharge cycle, the lithium ions are carried by the electrolyte through the separator from the anode to the cathode. This movement generates free electrons in the anode which creates a current from the positive current collector to the negative current collector. During the charging phase, the opposite happens.

To calculate the total mass of the battery necessary to power the airship the following equation was used:

$$m_{battery} = \frac{P_n \cdot t_f}{e} \quad (12)$$

where the term  $e$  refers to the energy stored in one kilogram of a battery (here, 260 Wh/kg). Using the model SLPB08008527 by Kokam as a reference, energy density was set as equal to 260 Wh/kg. The power provided by the battery system  $P_b$  can be estimated using Equation-13.

$$P_b = e \cdot m_{battery} \cdot C_{rate} \quad (13)$$

The term  $C_{rate}$  refers to the rate at which the battery is being discharged; here, it was set equal to 1. This could theoretically reach higher values up to 2, but it was set to a lower value to avoid extracting high-intensity currents, which would damage the operating life of the battery.

### 3.3 Supercapacitors.

Supercapacitors are a variation of the common capacitors with much higher energy densities. Capacitors are components capable of storing a certain amount of energy, in the form of a differential charge, when a current flows through it. With time, the current flowing in the capacitors exponentially tends toward zero and the capacitors reach their maximum charge. When a load is applied to a charged capacitor, the energy is consumed to provide a current flow to the load, powering it. A traditional capacitor is composed of two electrodes, separated by an insulating dielectric material. The fundamental equations governing this architecture are:

$$Q = CV \quad (14)$$

$$C = \epsilon_0 \epsilon_r \frac{A}{d} \quad (15)$$

$$E_{max} = \frac{1}{2} CV^2 \quad (16)$$

$$P_{max} = \frac{V^2}{4R_{ESR}} \quad (17)$$

where  $Q$  is the differential charge accumulated on the faces of the electrodes,  $C$  is the capacitance of the capacitor,  $V$  is the voltage applied to the electrodes,  $A$  is the area of those electrodes,  $d$  is the distance between them,  $\epsilon_0$  is the dielectric constant,  $\epsilon_r$  is the dielectric constant relative to the material used as a dielectric,  $R_{ESR}$  is the internal resistance of a capacitor,  $E_{MAX}$  is the maximum energy storables, and  $P_{MAX}$  the maximum power storables.

Common capacitors have very high specific powers, but low energy densities, resulting in very powerful, but brief, discharge. Supercapacitors try to increase this energy density by utilizing more efficient dielectrics, with a higher  $\epsilon_r$ , and more resistance to dielectric breaking (that occurs when the voltage applied to the capacitor is too high), and an incredibly higher electrode area. High electrode area and higher  $\epsilon_r$ , result in an increased capacitance (Equation-15); these changes do not affect the power provided by the capacitor (Equation-16) but increases the storables energy (Equation-17). These precautions, particularly the area increase, can be achieved by utilizing porous materials, such as opportunely treated carbon, immersed in an electrolyte solution. The voltage difference between the electrodes separates the charges of the solution, accumulating power. See Figure-3 for a schematic representation of a supercapacitor.

Supercapacitors show a briefly reduced power density, compared to traditional capacitors, but specific energies almost comparable to that of commercially used batteries. Supercapacitors have a great resistance to charge and discharge cycles compared to batteries but can maintain their charge for a lower amount of time. They are greatly effective as power buffers on any system that has to provide energy, absorbing or providing power to regularize the flow, as emergency power suppliers in case of blackouts instead of common batteries, and to absorb power peaks.

In airships the most important factor to minimize is weight. Due to the variability of the operating ambient, particularly imputable to wind variability and gusts, the power needed to operate the vehicle can vary greatly from phase to phase. Dimensioning an energy system capable of providing the peak power often results in excessive weight, and so a solution operating a supercapacitors module is essential. Load increase on the airship motors due to low duration gusts can be easily absorbed by such a system, providing a boost of energy when needed and recharging while operating at design conditions. Compared to a battery system, the supercapacitors show a lower degradation due to frequent charging and discharging caused by power peaks, and a lower charge and recharge time, resulting in lower masses required to provide the same power and high reactivity; making them the perfect choice for the energy system of the airship [26].

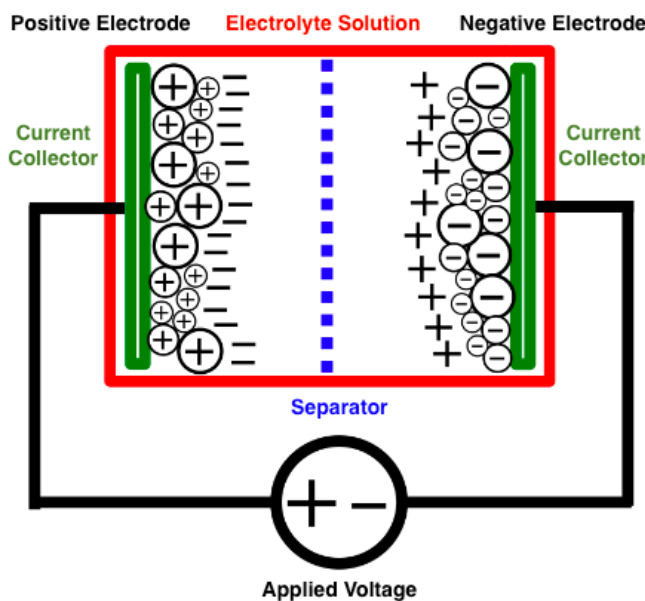


Figure 3 – Supercapacitor internal scheme

### 3.4 Optimal Sizing of the Onboard Energy System.

The code developed for sizing the energy system evaluates different sets of weight, volume, and power needed through an iterative and exhaustive research in the space of the variable parameters that define the airship. Those sets are determined from a range of values of four parameters: cruise flight speed, flight altitude, length of the airship, and relative thickness of the envelope. For each value of distance, the code saves the best configuration, i.e., the lightest one, which would also be the one with the smallest volume and with the least power needed. This procedure is repeated two times, one using the hydrogen fuel cell system and one using the battery system. At the end of the process the code prints two linear fits (one for each energy system configuration) showing how the total weight of the airship varies depending on the distance from the mission area. The best configuration, meant as the one that gives the lightest airship, is then selected according to the data shown in the graph.

The numerical code computes the total power, which includes the power needed to compensate the drag force at a certain cruise speed, to power the payload, and to control the attitude of the airship. It estimates the weight of the fuel cells using Equation-7. Then it calculates  $m_e$  and  $m_{H_2 \text{ tot}}$  with Equations-8, 10, and 11; before doing so, it is necessary to compute the value of  $t_f$ . Finally, the weight of the battery system  $m_{\text{battery}}$  is calculated using Equation-12.

The optimization procedure of the supercapacitor module uses a square wave model (Figure-4) to simulate the overall power curve required to operate the airship, and an electro-mathematical model (Figure-5) for the interrelation between the energy system, the supercapacitors module, and the various loads. In the proposed configuration only power exceeding nominal value must be absorbed by supercapacitors. The extra power is modelled as an intermittent power load, that requires constant power for a defined amount of time and activates at regular intervals. When this load is active the supercapacitors module must be able to sustain it with power, while when it is inactive the supercapacitors recharge by spilling energy from the energy system (energy that has to be considered in the dimensioning of the latter). For the sizing procedure, the relative increase in power of peaks with respect to the design conditions has been set to 200%, the peak duration to 30 seconds, and the total time occupied by peaks to 7% of  $t_f$ .

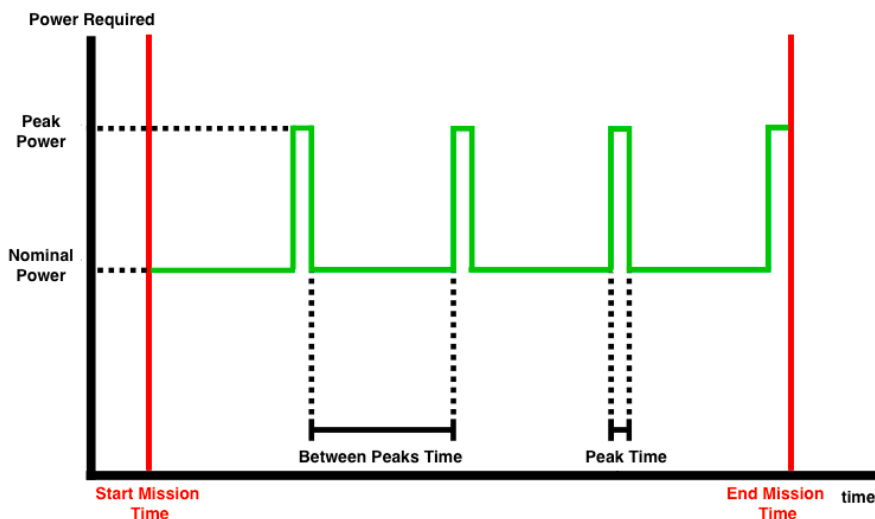


Figure 4 – Power curve along the mission time.

The sizing procedures use an optimization algorithm that, given the electrical model of the system, searches for the optimal supercapacitor module configuration in terms of weight. The supercapacitor module is essentially composed of a grid of supercapacitors in rows and columns. A grid of this kind, with some limitations, substantially works as a standalone supercapacitor, with different capacitance, internal resistance, and voltage. The algorithm iterates through a wide combination of supercapacitor types and configurations, respecting limitations of maximum voltage or current achievable with a specific type, searching for the lightest solution that satisfies two major requisites: the module must be able to power the intermittent load for the required time and to recharge itself without weighing too much on the energy system in terms of the power required in the time between peaks.

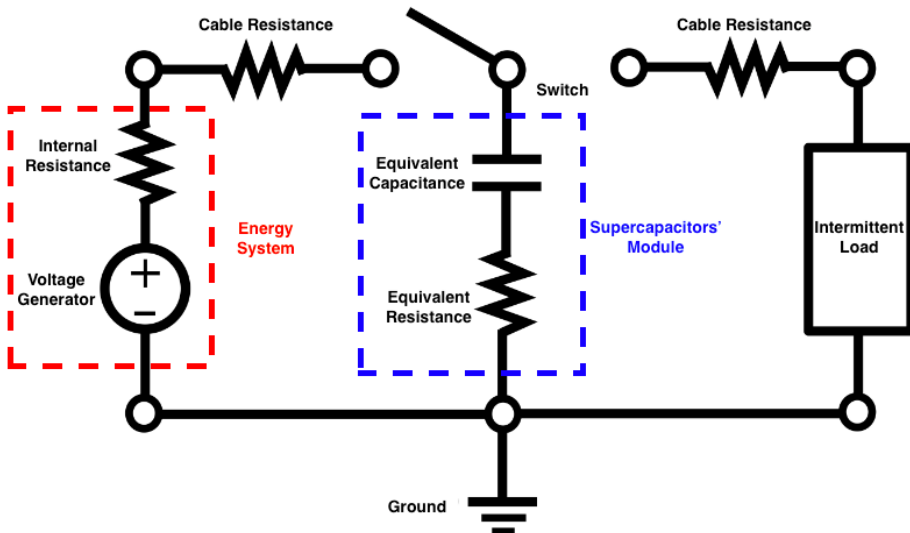


Figure 5 – Peak absorption electrical scheme

### 3.4.1 Results.

To determine the most convenient energy system configuration, the code saves, for both configurations, different distances from the revelation area and the respective weight of the airship that is necessary to complete the mission. Thanks to these data, it is possible to produce the two straight lines shown in Figure-6 by making a linear interpolation of the aforementioned set of values. It is noted that, in this analysis, the size of the detection area is set as constant and equal to  $10^7 m^2$ , which represents well the typical surface on which the airship will work.

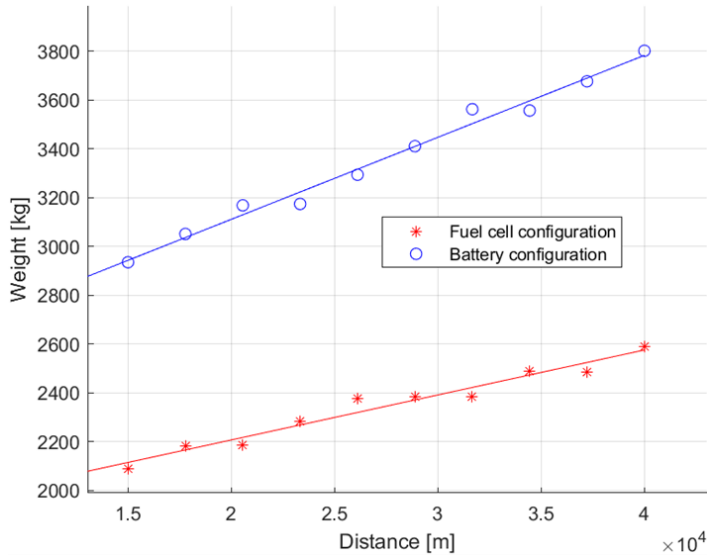


Figure 6 - Weights of the two systems vs distance.

The graph shows the significant advantages of using the fuel cells and hydrogen tank configuration: for example, when considering a distance equal to 15 km, the weight of the aircraft powered by fuel cells is approximately one-third less than the weight of the one using batteries. This gap becomes progressively bigger with the increase of the distance since the slope of the line relative to the battery configuration is steeper than the other one. According to this analysis the fuel cells and hydrogen tank configuration, for the type of mission considered, is by far the most convenient one in terms of weight. The reason why the weight was used as a reference to define the best configuration is that a minor weight means a smaller volume necessary to ensure the buoyancy, which also means less drag and less power necessary to compensate for it. By observing the slope of the two lines it appears that is possible to find a point below which the battery configuration is lighter, although it is for very low distances and a small detection area at which the utility of the airship may not be much relevant.

## 4. Propulsion and Control System.

The propulsion system of an airship is responsible for controlling the trajectory and orientation of the vehicle and typically relies on one or more propellers or ducted fans. In a standard configuration, the propellers generate the forward thrust while the horizontal and vertical tail stabilizers, with their relative control surfaces, control pitch, roll, and yaw manoeuvres while the aircraft is in motion. In the proposed configuration, a thrust vectoring approach (retrieved from previous projects, please refer to [27]) allows gaining control over multiple translational and rotational degrees of freedom of the motion of the airship, thus permitting more precise manoeuvres and also granting the possibility of hovering, where the aircraft maintains a fixed position relative to the ground. These aspects will be better discussed in a dedicated subsection.

The remotely controlled LTA platform can be operated from a Mobile Ground Station (MGS), which is not described here due to space constraints. Major details can be found in [28]. A nonlinear dynamic model can be used as a 12-state mathematical model for the flight simulator, needed for pilot training [29].

The numerical routine used for the sizing of the propulsion system starts from the assumed geometry and flight regime of the airship and computes the weight and power of the propulsion system, the propellers data and the onboard energy system data. The detailed procedure is presented in the following section.

### 4.1 Optimal Sizing for the Propulsion and Control System.

The sub-routine for the optimization of the propulsion subsystem takes as input parameters the airspeed of the airship  $u$ , the flight altitude  $z$ , the total displacement volume of the aircraft  $V$ , the relative thickness  $d/l$  of the envelope, and a flag corresponding to a particular mission phase (approach phase and survey phase are considered in the analysis). A chart of the optimization routine is presented in Figure-13.

Starting from these input parameters the drag coefficient relative to the volume  $C'_{DV}$  is calculated using Equation-4, and the following formula is used to calculate the Reynolds number  $Re$

$$Re = \frac{uL_{ref}\rho}{\mu} \quad (18)$$

For the air density  $\rho$  and viscosity  $\mu$ , the model of ISA (International Standard Atmosphere) is used.

The real drag coefficient is affected by the protruding elements of the airship and it is higher than the theoretical coefficient which only considers the shape of the hull. To keep the estimates conservative a loss coefficient is introduced such that:

$$C_{DV} = C'_{DV}k \quad (19)$$

where  $k = 1.5$ . This allows taking into account every component that modifies the chosen shape for the hull, e.g., the propeller-motor groups, the landing legs, and the payload bay.

A flight in a steady regime is then assumed for the general case sizing. Assuming constant airspeed it is possible to evaluate the necessary power  $P_{nec}$  generated by the propellers [30]

$$P_{nec} = \frac{1}{2}\rho u^3 C_{DV} V^3 \quad (20)$$

Knowing  $P_{nec}$  and the flight condition it is possible to optimize the propellers. The propeller optimization is carried out using the single propeller thrust,  $T$  derived by  $P_{nec}$ . Considering four propellers units, the single propeller thrust is

$$T = \frac{1}{4} \frac{P_{nec}}{u} \quad (21)$$

A separate exhaustive search is conducted to find the optimal geometry of the propeller. The space of parameters explored is defined by the propeller angular velocity  $\omega$ , the chord length of the blades  $c$ , the angle of attack of the blades  $\alpha$ , and the external radius of the propeller  $r_e$ .

For each combination of the search parameters, the performance of the propeller is evaluated using a Blade Element Momentum Theory (BEMT) model, which will be discussed more in detail in the next subsection. In this regard, it is ensured that the resultant thrust is greater or equal to the input thrust  $T$ , used as a project parameter. Out of every acceptable solution found the propeller having higher

efficiency is chosen.

The effective power consumed by the electric motors  $P_{mot}$  is evaluated considering two efficiency coefficients:

$$P_{mot} = \frac{P_{nec}}{\eta_{prop}\eta_{mot}} + P_{lift} \quad (22)$$

where  $\eta_{prop}$  is the propeller efficiency, returned by the propeller optimization,  $\eta_{mot}$  is the efficiency of the electric motors and mechanical transmission and  $P_{lift}$  is the power that needs to be supplied to the two motors that drive the two vertical axis propeller, this last term is independent of the airspeed and is assumed a constant in this analysis. Table-3 presents the estimates for efficiency and power used in the sizing study.

Table 3 - Estimated parameters.

Parameter symbol	Estimate
$\eta_{mot}$	0.9
$P_{lift}$	2000 W

To calculate the total power consumed by the airship, the power used to control the navigation needs to be added. The control of the navigation is performed by regulating the propellers' orientation using electric stepper motors, controlled by the centralized flight controller. The power consumed by this system is highly variable, thus a time average estimate of 2000 W is chosen. For dimensioning the propulsive system during the survey phase of the mission, the sub-routine must consider the power consumed by the payload as well. The peak power consumption by the payload was estimated to about 1000 W. Power data are used for the dimensioning of the onboard energy system. Another important factor of the propulsion system which influences the overall dimensioning is the weight, which in the same way as every other subsystem, affects the displacement volume of the airship. To evaluate the weight of this subsystem a linear dependence with power is assumed, the estimate of the subsystem specific power is conservatively set at 300 W/kg [31].

#### 4.1.1 Blade Element Momentum Theory (BEMT).

BEMT is a mathematical model that allows the evaluation of the performance of rotating blades in machines like wind turbines, turbomachines, or propellers. The model is derived from two lower-order theories: Blade Element Theory (BET) and Momentum Theory (MT). For completeness, a brief summary of the two models is included here.

The MT starts from the actuator disc theory and introduces two correction factors  $a$  and  $b$  for the velocity of the air through the propeller disc. The thrust  $dT$  and resistant torque  $dC$  relative to an annulus of the propeller disc having infinitesimal width  $dr$  [32] are

$$dT = 4\pi[(1+a)a]\rho r u^2 dr \quad (23)$$

$$dC = 4\pi[(1+a)b]\rho r^3 \omega u dr \quad (24)$$

where  $r$  is the radial position of the annulus,  $a$  is the axial induction factor, and  $b$  is the rotational induction factor. They are a dimensionless form of the axial velocity increment on the propeller disc  $u_0$  and the angular velocity of the wake formed downstream of the propeller disc

$$a = \frac{u_0}{u} \quad (25)$$

$$b = \frac{\omega_{wake}}{2\omega} \quad (26)$$

The factors  $a$  and  $b$  are unknown and can be computed only by introducing the BET.

BET considers a radial portion of the propeller blades with thickness  $dr$  (called blade element) and approximates the flow around a blade element using 2D airfoil theories. BEMT supposes that the airfoil geometry of the blade and the number of blades in the propeller  $N_b$  are already set from the start. Drag coefficient  $C_D$  and lift coefficient  $C_L$  of the airfoil also need to be evaluated before the application of this model.

Considering the tangential velocity  $\omega r(1 - b)$  and axial velocity  $u(1 + a)$  of the flow seen by the blade, it can be shown that the thrust  $dT$  and torque  $dC$  of a blade element correspond to [33]

$$dT = \frac{N_b}{2} \rho W^2 c(C_L \cos \varepsilon - C_D \sin \varepsilon) dr \quad (27)$$

$$dC = \frac{N_b}{2} \rho W^2 cr(C_L \sin \varepsilon - C_D \cos \varepsilon) dr \quad (28)$$

Where the inflow angle  $\varepsilon$  and the relative airspeed  $W$  can be computed as

$$\varepsilon = \tan^{-1} \left( \frac{u(1 + a)}{\omega r(1 - b)} \right) \quad (29)$$

$$W = \sqrt{[V(1 + a)]^2 + [\omega r(1 - b)]^2} \quad (30)$$

See Figure-7 for further clarifications.

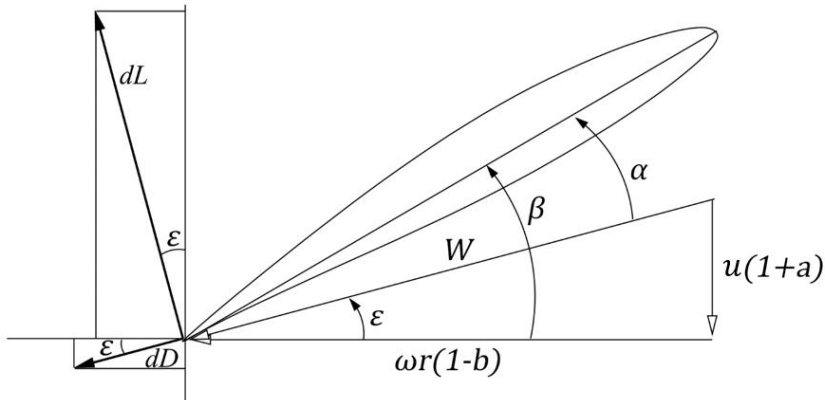


Figure 7 - Airfoil in the BET

The BEMT model combines the thrust and torque evaluated by these two models and derives a system of two equations, having  $a$  and  $b$  as unknown variables. It is possible to solve this system separately for every different blade element in which the blade has been discretized. After knowing  $a$  and  $b$  every other parameter can be obtained.

$$\begin{cases} \frac{N_b}{2} \rho W^2 c(C_L \cos \varepsilon - C_D \sin \varepsilon) = 4\pi[(1 + a)a] \rho r u^2 \\ \frac{N_b}{2} \rho W^2 cr(C_L \sin \varepsilon - C_D \cos \varepsilon) = 4\pi[(1 + a)b] \rho r^3 \omega u \end{cases} \quad (31)$$

The main limitation of the BEMT model is the hypothesis that every blade element does not influence the performance of contiguous elements. This limitation is particularly evident in the tip and hub portion of the blades, where the interaction of the flow with tip vortices and the propeller nose cone, respectively, highly affects performance. To include these observations in the model two corrective factors  $F_h$  and  $F_t$  are implemented, scaling down the thrust and torque resulting from the MT part of the equations.

The factors  $F_h$  and  $F_t$  usually derive from both experimental data and analytical models. The model implemented the expression originally proposed by Moriarty, Hansenl and Glauert and described in [34]. Thus,  $F_t$  and  $F_h$ , are respectively defined as:

$$F_t = \frac{2}{\pi} \cos^{-1} \left( e^{-\frac{N_p}{2} \frac{r_e - r}{r \sin \varepsilon}} \right) \quad (32)$$

$$F_h = \frac{2}{\pi} \cos^{-1} \left( e^{-\frac{N_p}{2} \frac{r - r_{hub}}{r \sin \varepsilon}} \right) \quad (33)$$

The final BEMT system is:

$$\begin{cases} \frac{N_b}{2} \rho W^2 c(C_L \cos \varepsilon - C_D \sin \varepsilon) = 4\pi[(1 + a)a] \rho r u^2 F_h F_t \\ \frac{N_b}{2} \rho W^2 cr(C_L \sin \varepsilon - C_D \cos \varepsilon) = 4\pi[(1 + a)b] \rho r^3 \omega u F_h F_t \end{cases} \quad (34)$$

The numerical sizing procedure starts from the necessary thrust to achieve flight at cruise airspeed, evaluated by the numerical model at every iteration. This value is used as a requirement for propeller sizing. For the optimal airship, the necessary thrust, corrected with a safety factor of 1.6, for every propeller is  $T_{req} = 343.75$  N. During the exhaustive search of the optimal propeller, other than the constraint of the minimum thrust required, a geometrical constraint is also imposed. For constructional and structural reasons, the maximum radius of the propellers is set to 1.5 m.

A preliminary study conducted using the propeller radius and the propeller angular velocity as variable parameters established that, due to the low cruise velocities, the optimal propeller is characterized by low angular velocities and high diameters. The strictest constraint in this sense is the geometrical limitation of the dimension of the propeller and to maximize performance the preliminary study used the highest possible dimension available. Thus, the external radius of the propeller was set to 1.5 m for the subsequent computations.

The airfoil chosen for the implementation is a NACA 4412 airfoil, and its aerodynamic data was computed before the numerical implementation using the software XFOIL. The choice of this specific airfoil was motivated by data availability reasons and because it is a simple and well-known profile whose behaviour could be easily predicted.

#### 4.1.2 Thrust Vector Control.

A thrust vector control system on an airship relegates the need for stabilizers and allows flight configurations otherwise impossible on an airship, like hover flight, lateral translation flight, and backward flight. For a remote sensing airship, this means that during the survey part of the missions a flight path of any shape can be followed, without rotating the airship with respect to the ground, thus saving time and resources.

In the proposed design the thrust outputted by any of the six propellers can be regulated by controlling the angular velocity of the electric motors power shafts. To perform the different manoeuvres the four horizontal axis propeller steering capabilities are used (see Figure-8).

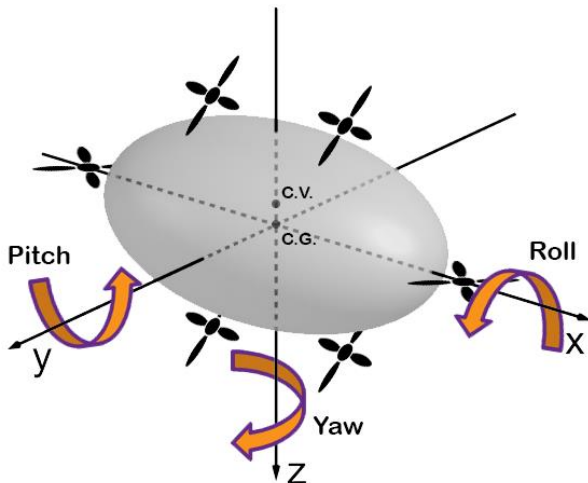


Figure 8 - Rotational degrees of freedom of a thrust vectoring airship

Stepper motors are ideal for this application because high angular position precision is required and the motor must also be capable of maintaining a set position, even with external perturbation.

The dimensioning of stepper motors is conducted starting from a mathematical model of the motor-propeller group that needs to be steered, which is an approximation, using simple geometric solids, of the supposed architecture (Figure-9). The forces considered in the analysis are the aerodynamic drag  $D$ , the thrust  $T$ , and the wind pressure  $P_v$ .

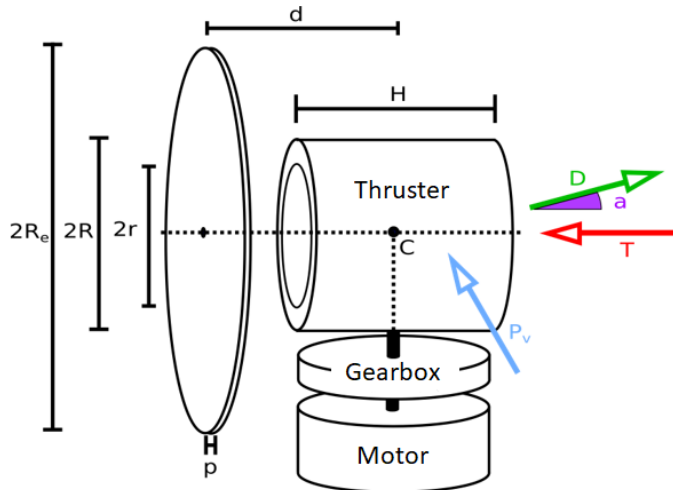


Figure 9 - Geometrical model of the propulsive system

A dedicated algorithm searches from a wide model selection of steppers, searching for the weight-optimizing solution, considering that the stepper must be able to steer the electrical motor even against strong perturbations caused by wind and inertial forces. The code considers an aluminium capsule casing to maintain the stepper in place against wind and other forces, whose weight must also be considered.

#### 4.1.3 Results.

The data of the propulsive subsystem are summarized in Table-4. The values refer to the optimal configuration found via the numerical model. For reasons already discussed only the fuel cell configuration is taken into account.

Table 4 – Optimal propulsive system configuration data.

Parameter name	Parameter symbol	Value
Airship drag coefficient relative to the volume	$C_{DV}$	0.0371
Total propulsion system power in a steady flight regime	$P_{tot}$	15100 W
Total propulsion system mass	$m_{propulsion}$	40.0 Kg
Cruise airspeed velocity	$u$	11.7 m/s

Studying the performance of propellers for different radii and angular velocities it can be seen that the points of maximum efficiency are located around low values of angular velocities, and high values of external radius (Figure-10). However, studying propellers with a radius of 1.5 m and excluding from the charts the ones that do not satisfy the requirement of minimum thrust  $T_{req} = 343.75$  N, only a reduced set satisfies this constraint (Figure-11). The reason behind this observation is that the airship flies at low cruise speeds, especially when compared to fixed-wing aircraft, thus moving the point of maximum efficiency towards large, low rotation propellers.

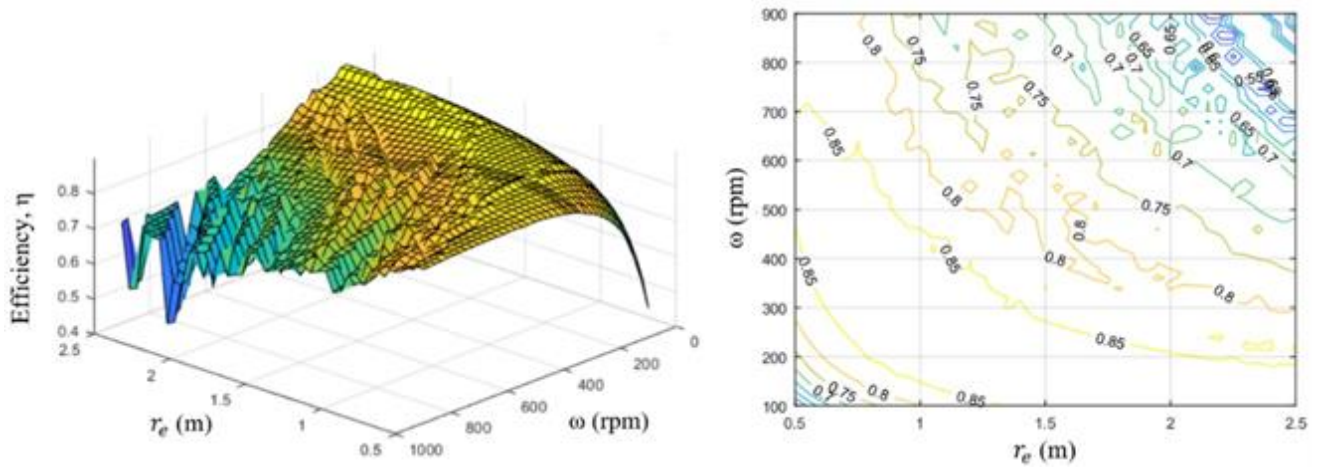


Figure 10 - Surface plot (left) and contour plot (right) of  $\eta_{prop}$  as function of  $\omega$  and  $r_e$ .

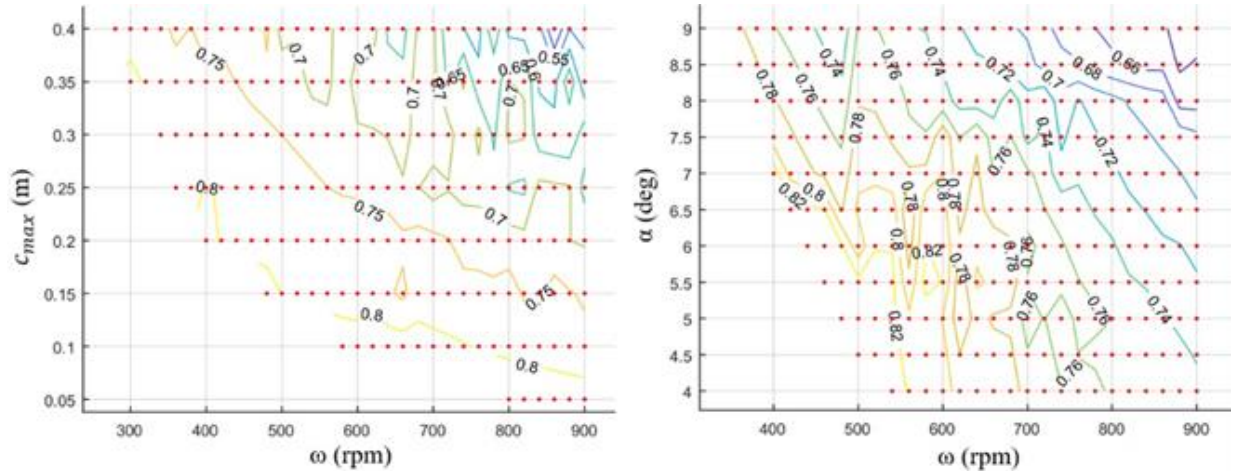


Figure 11 - Contour plot of  $\eta_{prop}$  of the propellers which satisfy the thrust requirement as a function of  $\omega$  and  $c$  (left), and as function of  $\omega$  and  $\alpha$  (right).

Because of these constraints, the proposed propellers cannot function at their maximum efficiency points with sufficient thrust, therefore the optimal propeller for this application has lower nominal efficiency and works at higher rpm.

The data of the propeller of maximum efficiency which also satisfies every constraint are listed in Table-5, while in Figure-12 the geometry of the blades of the optimal propeller is shown.

Table 5 - Optimal propeller data.

Parameter name	Parameter symbol	Value
Propeller external radius	$r_e$	1.50 m
Number of blades	$N_b$	2
Propeller nominal angular velocity	$\omega$	500 rpm
Maximum chord of the airfoil	$c_{max}$	0.150 m
Design angle of attack of the blades	$\alpha$	6.00 °
Propeller advance ratio	$J$	0.204
Propeller efficiency	$\eta_{prop}$	0.847
Thrust	$T$	353 N
Torque	$C$	127 Nm

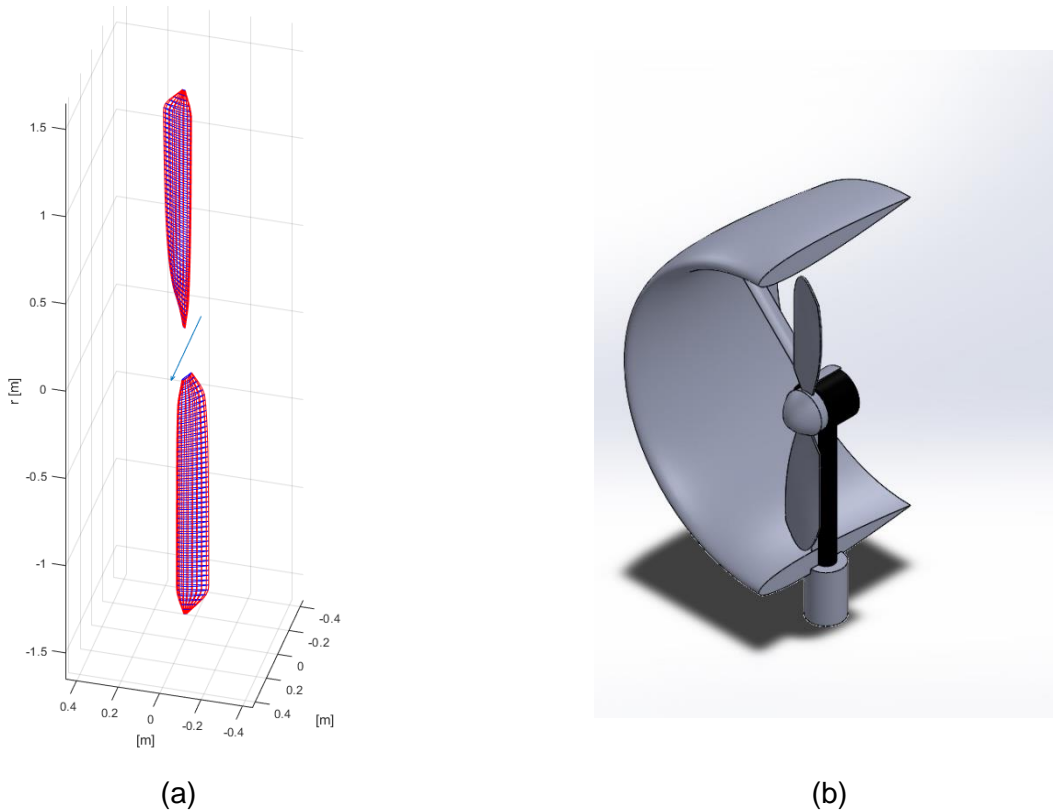


Figure 12 – (a): blade geometry of the optimal propeller. (b): cutaway drawing (isometric view).

## 5. Discussion.

The optimisation of the energy, control, and propulsion systems returned the two mass breakdowns portrayed in Figure-13 (for the 34 m-long configuration).

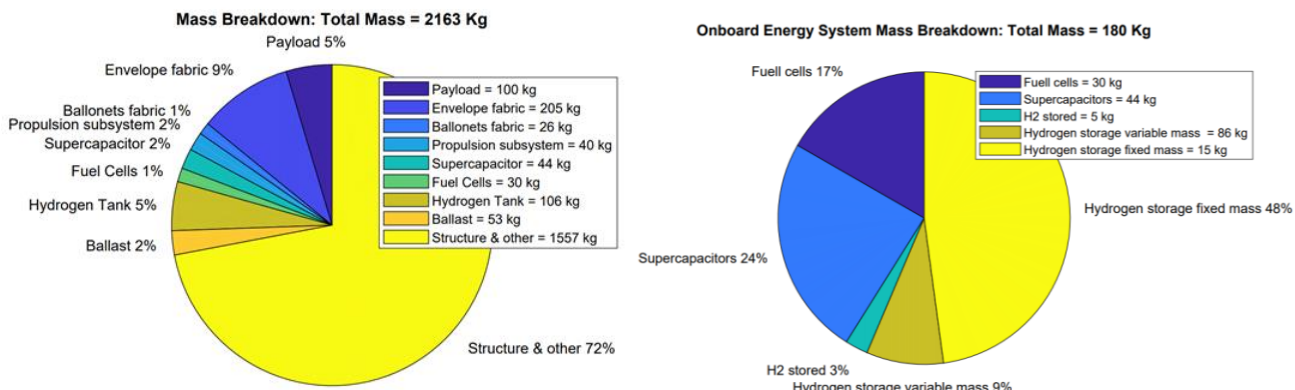


Figure 13 - Mass breakdown of the optimal fuel cells powered airship, having a total length of 34 m (left) and mass breakdown of the onboard energy system (right).

Figure-13 shows that the heaviest component of the airship is the structure, which contributes to more than two-thirds of the total weight, while other significant contributions come from the envelope, payload and hydrogen tank, despite being an order of magnitude lower than the structure. Moreover, the graph outlines that the heaviest element of the energy system is the hydrogen tank, especially its variable masses, while the  $H_2$  only weights 3% of the total system. This demonstrates what was mentioned before about the criticalities of the compressed hydrogen storage solutions. Therefore, is notable that the supercapacitor module contributes only to 24% of the total energy system weight, but is capable of providing the same power, for brief intervals, to cover for the power peaks. Their presence allows for a lighter energy system than a configuration without them would require.

Regarding the optimization of the propeller, the main result obtained is that, at low cruise speed, to maximize efficiency large radius and low rotations propeller should be employed. In the propulsion system analysis, however, the weight of the system is assumed linear to the power necessary to move the airship, and no other estimates for propeller weight are used. Propellers with a large radius, other than having a heavier contribution to the total weight, also affect the sizing of the stepper motor system needed for the navigation. Despite this, the stepper sizing procedure uses a reference mean weight for the propellers to simplify the analysis. For a more accurate evaluation of the optimal propeller, the propeller mass as a function of its radius should also be considered.

The sizing procedure considers two-blade propellers, however resorting to a ducted propeller is more efficient than an unducted alternative at low speeds and can produce more thrust in a smaller package. In the preliminary design phase, the sizing process can be assumed independent by the propeller being ducted or not. A NACA 0012 airfoil was selected for the duct profile.

The flow chart of the complete optimisation routine which led to these results is reported in Figure-14. Please note that  $SH$  refers to the static heaviness of the airship, defined as the amount by which the LTA aircraft's weight exceeds buoyancy; in the optimal configuration for the airship this is equal to 2%.

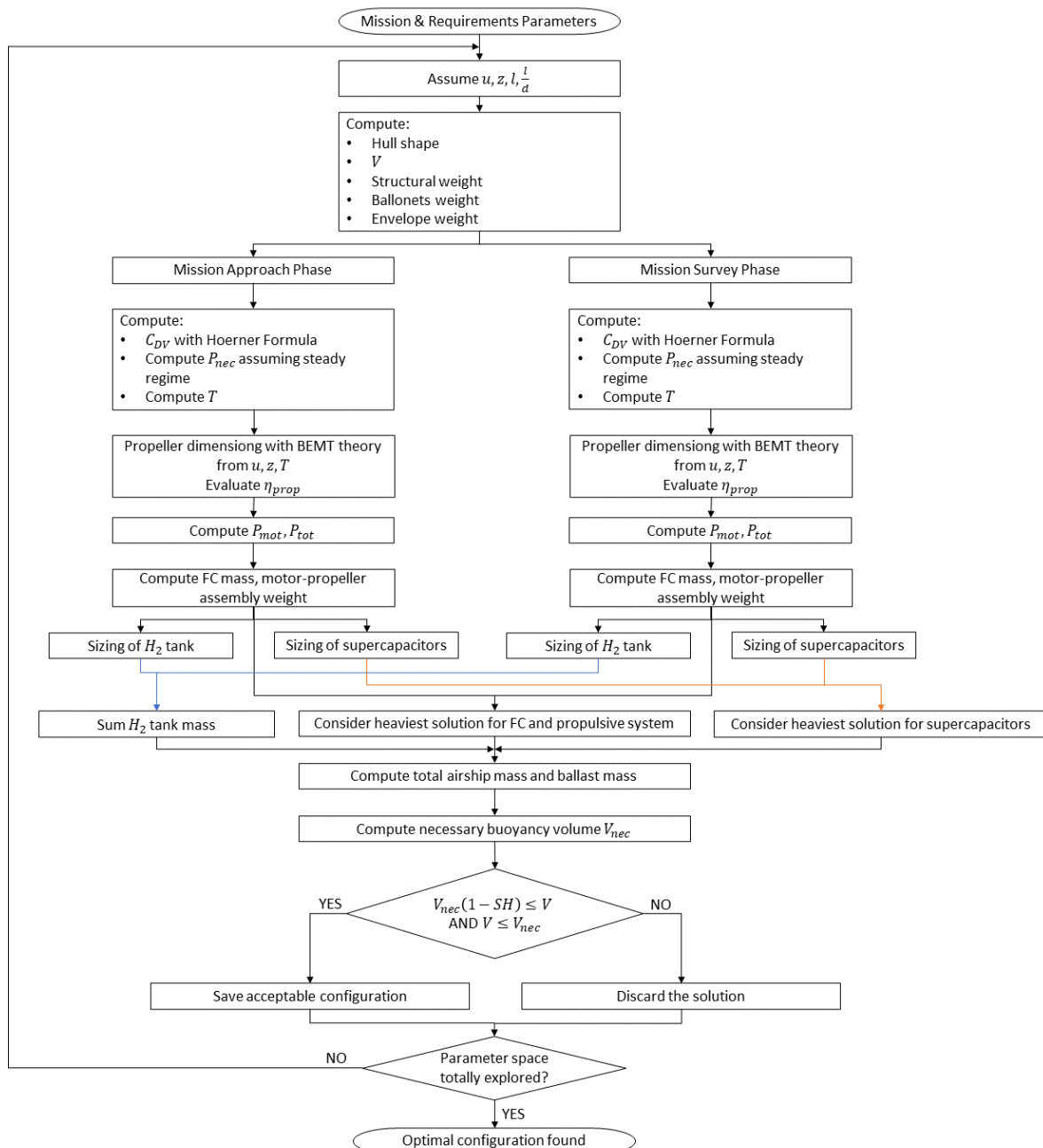


Figure 14 - Flow chart of the numerical routine.

## 6. Conclusions.

The proof of feasibility conducted in this work shows that a Lighter Than Air (LTA) vehicle for remote sensing is capable of filling a gap in the field of remote sensing applications, competing with vehicles such as drones, helicopters, aeroplanes, and satellites. Indeed, an airship has a payload capacity much higher than most common remotely controlled UAVs and has lower operative costs and a lower carbon footprint than aircraft and satellites. This study also demonstrated that a full electric, zero-emission solution is feasible, with a combination of hydrogen fuel cells and supercapacitors for the power sources. A thrust-vectoring configuration for the propulsive system helps to maintain low survey times and improves the versatility of the vehicle. The system needs to be paired with appropriate propellers whose dimensions increase as cruise speed decreases.

The main application of a remote sensing LTA vehicle with an optical payload is Land Use and Land Control surveys. In this regard, it is of particular interest the possibility to fly under the level of clouds, potentially allowing operativity in days with non-optimal weather conditions. LULC monitoring is a valuable tool for keeping track of human impact effects on the environment and for conduction risk assessment of natural disasters like floods, or fires. Finally, the multidisciplinary optimisation scheme followed in this and related works showed great potential for the automatic design of LTA platforms. However, further research will be needed for this specific aim.

Future developments of the work can be carried out exploring different airship configurations to further improve the survey area of one mission, here preliminarily set at  $10 \text{ km}^2$  by way of example, and the operative range of the vehicle which, for a standard mission, is considered to be about 10 km.

## 7. Contact Author Email Address

Mail to: marco.civera@polito.it

## 8. Copyright Statement

The authors confirm that they, and/or their company or organization, hold copyright on all of the original material included in this paper. The authors also confirm that they have obtained permission, from the copyright holder of any third party material included in this paper, to publish it as part of their paper. The authors confirm that they give permission, or have obtained permission from the copyright holder of this paper, for the publication and distribution of this paper as part of the ICAS proceedings or as individual off-prints from the proceedings.

## 9. Acknowledgements

The Authors would like to thank the Interdepartmental Responsible Risk Resilience Centre (R3C) of Politecnico di Torino, Turin, Italy for the support of this project.

## References

- [1] Garg A., Burnwal S., Pallapothu A., Alawa R. and Ghosh, A. Solar panel area estimation and optimization for geostationary stratospheric airships. *11th AIAA Aviation Technology, Integration, and Operations (ATIO)*, Virginia Beach, VA, USA, 2011.
- [2] Liao J., Jiang Y., Li J., Liao Y., Du H., Zhu W. and Zhang L. An improved energy management strategy of hybrid photovoltaic/battery/fuel cell system for stratospheric airship. *Acta Astronautica*, Vol. 152, pp 727-739, 2018.
- [3] Liao L., Pasternak I. A review of airship structural research and development. *Progress in Aerospace Sciences*, Vol. 45, No. 4–5, pp 83–96, 2009.
- [4] P. Gili, R. Roy, M. Civera, D. Allaio, R. Barbieri, A. Grava, R. Tufilli, and C. Surace. Design of a prototype unmanned lighter-than-air platform for remote sensing: structural design and optimization. *Presented at the 32nd congress of the International Council of the Aeronautical Sciences (ICAS)*, Shanghai, China, August 2021.
- [5] Mueller J., Paluszek M., and Zhao Y. Development of an Aerodynamic Model and Control Law Design for a High Altitude Airship. *Presented at AIAA Unmanned Unlimited Conference*, Chicago, Illinois, USA, 2004.
- [6] Dorrington G. E. Drag of spheroid-cone shaped airship. *Journal of Aircraft*, Vol. 43, No. 2, March–April 2006.
- [7] Zhang Y. Photogrammetric processing of low altitude image sequences by unmanned airship. *The International Archives of the Photogrammetry, Remote Sensing and Spatial Information Sciences*, pp 37, 751-757, 2008.
- [8] Zongjian L. UAV for mapping-low altitude photogrammetric survey. *International Archives of Photogrammetry and Remote Sensing*, Beijing, China, pp 37, 1183-1186, 2008.
- [9] Ren P., Meng Q., Zhang Y., Zhao L., Yuan X., and Feng X. An unmanned airship thermal infrared remote sensing system for low-altitude and high spatial resolution monitoring of urban thermal environments: integration and an experiment. *Remote Sens*, Vol. 7, No. 11, pp 14259-14275, November 2015.
- [10] Vallet J. GPS/IMU and LiDAR integration to aerial photogrammetry: development and practical experiences

- with helimap system. *ISPRS ICWG I/V UAV-g (unmanned aerial vehicle in geomatics) conference*, Zurich, Switzerland, 2011.
- [11] Koska B., Jirka V., Urban R., Křemen T., Hesslerová P., Jon J., Pospíšil J., and Fogl M. Suitability, characteristics, and comparison of an airship UAV with lidar for middle size area mapping. *International Journal of Remote Sensing*, Vol. 38, No. 8-10, pp 2973-2990, 2017.
  - [12] Liu Z., Wu J., and Yang H. Developing unmanned airship onboard multispectral imagery system for quick-response to drinking water pollution. *MIPPR 2009: Multispectral Image Acquisition and Processing*, Vol. 7494, p. 74940L, October 2009.
  - [13] Choi C. U., Kim Y. S., and Nam K. W. The study of environmental monitoring by science airship and high accuracy digital multi-spectral camera. *Proceedings of the KSRS (The Korean Society of Remote Sensing) Conference*, pp. 750-750, 2002.
  - [14] Yang P., Liu Z., Wang Q., Zhang W. Solar-induced chlorophyll fluorescence extraction and validation at airborne level based on an unmanned airship. *Guang Pu Xue Yu Guang Pu Fen Xi = Guang Pu*, Vol 33, No. 11, pp 30101-3105, 2013.
  - [15] Hu S., Zhang A., and Chai S. Multi-payload observation system from high altitude airship. *IEEE Sensors Journal*, Vol. 19, No. 24, Dec. 2019.
  - [16] Retzlaff, Rebecca. On the potential of small UAS for multispectral remote sensing in large-scale agricultural and archaeological applications. *Vom Fachbereich VI (Raum- und Umweltwissenschaften) der Universität Trier, zur Erlangung des akademischen Grades Doktor der Naturwissenschaften*, 2016.
  - [17] Civera, M., and Surace, C. A comparative analysis of signal decomposition techniques for structural health monitoring on an experimental benchmark. *Sensors*, Vol 21, No 5, pp 1825, 2021.
  - [18] Ferraris, M., Civera, M., Ceravolo, R., Surace, C., and Betti, R. Using enhanced cepstral analysis for structural health monitoring. *Proceedings of the 13th International Conference on Damage Assessment of Structures*, pp 150-165, 2020.
  - [19] Martucci, D., Civera, M., and Surace, C. The extreme function theory for damage detection: an application to civil and aerospace structures. *Applied Sciences*, Vol 11, No 4, pp 1716, 2021.
  - [20] Battipede, M., Gili, P., Maggiore, P., and Lando, M. Risk assessment and failure analysis for an innovative remotely-piloted airship. *6th AIAA Aviation Technology, Integration and Operations Conference (ATIO)*, pp 7716, 2006.
  - [21] Zhang F., Zhao P., Niu M., and Maddy J. The survey of key technologies in hydrogen energy storage. *International Journal of Hydrogen Energy*, Vol. 41, No. 33, pp 14535–14552, 2016.
  - [22] Sürer M., Arat H. State of art of hydrogen usage as a fuel on aviation. *European Mechanical Science*, Vol. 2, pp 20-30, 2018.
  - [23] Adam J., Houchins C., Ahluwalia R. Onboard Type IV Compressed Hydrogen Storage System – Cost and Performance Status. *Department of Energy USA, DOE Hydrogen and Fuel Cells Program Record*, Record 19008, 2019.
  - [24] Gong A., Verstraete D. Fuel cell propulsion in small fixed-wing unmanned aerial vehicles: Current status and research needs. *International Journal of Hydrogen Energy*, Vol. 42, No. 33, pp 21311-21333, 2017.
  - [25] Scrosati B., Garche J. Lithium batteries: Status, prospects and future. *Journal of Power Sources*, Vol. 195, No. 9, pp 2419-2430, 2010.
  - [26] Halper M. S., Ellenbogen J. C. Supercapacitors: a brief overview, *MITRE Nanosystem Group*, March 2006.
  - [27] Battipede M., Lando M., and Gili P. Mathematical modelling of an innovative unmanned airship for its control law design. *IFIP Int. Fed. Inf. Process.*, Vol 202, pp 31–42. 2006.
  - [28] Battipede, M., Gili, P., and Lando, M. Ground station and flight simulator for a remotely-piloted non conventional airship. *AIAA guidance, navigation, and control conference and exhibit*, pp 6201. 2005
  - [29] Gili, P., Lerro, A., Vazzola, M., and Visone, M. A New Approach for the Estimation of the Aerodynamic Damping Characteristics of the ETF Demonstrator. *SAE International Journal of Aerospace*, Vol 4, pp 1115-1124, 2011.
  - [30] Khouri G. A., Gillett J. D. Airship technology. *Cambridge University Press*, 2012.
  - [31] Liang H., Zhu M., Guo X., and Zheng Z. Conceptual design optimization of high altitude airship in concurrent subspace optimization. *50th AIAA Aerospace Sciences Meeting including the New Horizons Forum and Aerospace Exposition*, Nashville, Tennessee, January 2012.
  - [32] Winarto H. BEMT algorithm for the prediction of the performance of arbitrary propellers. *The Sir Lawrence Wackett Centre for Aerospace Design Technology, Royal Melbourne Institute of Technology*, March 2004.
  - [33] Ramdin S.F. Prandtl tip loss factor assessed. *Master of Science Thesis For obtaining the degree of Master of Science in Aerospace Engineering at Delft University of Technology*. Faculty of Aerospace Engineering, Delft University of Technology, January 2017.
  - [34] Masters I., Chapman J., Orme J., Willis M. A robust blade element momentum theory model for tidal stream turbines including tip and hub loss corrections. *Proceedings of IMarEST - Part A - Journal of Marine Engineering and Technology*, Vol. 10, No. 1, pp 25-35, January 2011.